

# Chitosan-CdS Quantum Dots Biohybrid for Highly Selective Interaction with Copper(II) Ions

Faisal K. Algethami,\* Ilyes Saidi, Hichem Ben Jannet, M. Khairy, Babiker Y. Abdulkhair, Youssef O. Al-Ghamdi, and Hani Nasser Abdelhamid\*



Cite This: *ACS Omega* 2022, 7, 21014–21024



Read Online

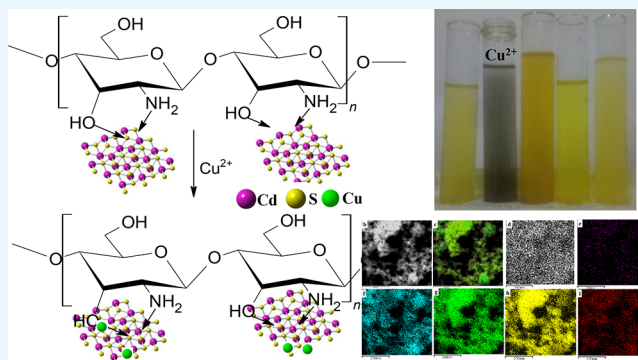
ACCESS |

Metrics & More

Article Recommendations

Supporting Information

**ABSTRACT:** Cadmium sulfide (CdS) quantum dots (QDs) were homogeneously embedded into chitosan (CTS), denoted as CdS@CTS, via an in situ hydrothermal method. The intact structure of the synthesized materials was preserved using freeze-drying. The materials were characterized using X-ray diffraction (XRD), X-ray photoelectron spectroscopy, transmission electron microscopy, high-resolution TEM, scanning TEM, dispersive energy X-ray (EDX) for elemental analysis and mapping, Fourier transform infrared spectroscopy, nitrogen adsorption–desorption isotherms, thermogravimetric analysis, UV–vis spectroscopy, and diffuse reflectance spectroscopy (DRS). The synthesis procedure offered CdS QDs of 1–7 nm (average particle size of 3.2 nm). The functional groups of CTS modulate the in situ growth of CdS QDs and prevent the agglomeration of CdS QDs, offering homogenous distribution inside CTS. CdS@CTS QDs can also be used for naked-eye detection of heavy metals with high selectivity toward copper ( $\text{Cu}^{2+}$ ) ions. The mechanism of interactions between  $\text{Cu}^{2+}$  ions and CdS@CTS QDs were further studied.



and copper (II) ions. The mechanism of interactions between  $\text{Cu}^{2+}$  ions and CdS@CTS QDs were further studied.

## INTRODUCTION

Bipolymers such as cellulose and chitin are promising for several applications.<sup>1–5</sup> Chitosan (CTS, with a chemical name of (1,4)-2-amino-2-deoxy- $\beta$ -D-glucan) is a natural and abundant biopolymer.<sup>6–10</sup> It is the deacetylated form of chitin that can be isolated from crustacean shells. It exhibits several properties such as high biocompatibility, biodegradability, and mucoadhesive properties. Chitosan biopolymers can be used as effective templates, supports, or substrates to synthesize several nanomaterials, including photocatalysts,<sup>11</sup> magnetic nanoparticles,<sup>12–14</sup> molybdenum vanadate,<sup>15</sup> metal–organic frameworks (MOFs),<sup>16–18</sup> and graphene oxide (CTS).<sup>19</sup> Chitosan-based materials enable several applications, e.g., separation, photocatalysis, biotechnology, and biosensing applications.<sup>10,20–23</sup>

Quantum dots (QDs) or semiconductor nanocrystals (SNCs) exhibited unique optical and electronic properties, making them distinct from other nanomaterials.<sup>24–36</sup> QDs show good luminescence properties compared to organic and inorganic nanoparticles.<sup>15,37–41</sup> The emission wavelength of QDs can be modified via the changing in QDs' particle size or by selecting a suitable light source for excitation.<sup>42–46</sup> QDs exhibit a narrow, tunable, and symmetric emission spectrum compared to organic fluorophores.<sup>47,48</sup> However, QDs with small capping agents tend to aggregate or agglomerate. Thus, large molecules such as biopolymers can be used as stabilizers

and capping agents for QDs. The functional groups in the biopolymers can interact with target species such as heavy metal ions offering adsorption and biosensing applications. Several biomolecules were reported to synthesize QD bioconjugates.<sup>49–52</sup> However, some of these biomolecules exhibit weak interaction with QDs causing agglomeration or aggregation during the material's separation or under storage as an aqueous solution. Furthermore, preparing these QD bioconjugates requires complicated procedures and sometimes lacks high reproducibility. The ability to conjugate QDs into biopolymer assemblies such as CTS could create several opportunities for scientific discovery.<sup>53–57</sup> The surface modification of QDs using biopolymers such as CTS improves the biocompatibility of QDs.<sup>58</sup>

Herein, cadmium sulfide (CdS) QDs was obtained via the reaction of sodium sulfide ( $\text{Na}_2\text{S}$ ) with a Cd-coordinated chitosan ( $\text{Cd}^{2+}$ @CTS) solution under stirring at a mild temperature (90 °C). The prepared material, i.e., CdS@CTS QDs, was dried via the freeze-drying method. CdS@CTS QDs

**Received:** March 24, 2022

**Accepted:** May 17, 2022

**Published:** June 7, 2022



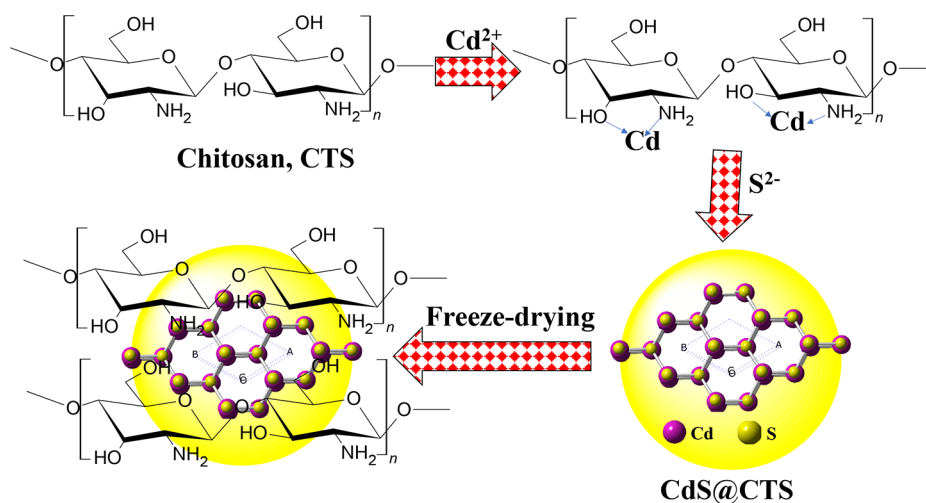


**Figure 1.** Schematic representation for the synthesis of CdS@CTS QDs.

were analyzed using X-ray diffraction (XRD), transmission electron microscopy (TEM), high-resolution TEM image (HR-TEM), scanning TEM (STEM), energy-dispersive X-ray (EDX) analysis/mapping, Fourier transforms infrared (FT-IR) spectroscopy, X-ray photoelectron spectroscopy (XPS), nitrogen adsorption/desorption isotherm, diffuse reflectance spectroscopy (DRS), and thermogravimetric analysis (TGA). It was applied for the chemosensing of heavy metal ions. It showed higher selectivity toward copper ( $\text{Cu}^{2+}$ ) ions than other metal ions. The interaction mechanism between CdS@CTS QDs and  $\text{Cu}^{2+}$  ions was supported with experimental data such as TEM, HR-TEM, STEM, EDX analysis/mapping, DRS, FT-IR, and XPS.

## EXPERIMENTAL SECTION

**Materials and Methods.** Chitosan (CTS, high molecular weight, *N*-deacetylation 75%) was purchased from Sigma-Aldrich (Germany). Cadmium nitrate ( $\text{Cd}(\text{NO}_3)_2$ ), copper sulfate ( $\text{CuSO}_4$ ), zinc nitrate ( $\text{Zn}(\text{NO}_3)_2$ ), calcium nitrate ( $\text{Ca}(\text{NO}_3)_2$ ), nickel nitrate ( $\text{Ni}(\text{NO}_3)_2$ ), cobalt chloride ( $\text{CoCl}_2$ ), magnesium nitrate ( $\text{Mg}(\text{NO}_3)_2$ ), ferrous sulfate ( $\text{FeSO}_4$ ), sodium chloride ( $\text{NaCl}$ ), potassium chloride ( $\text{KCl}$ ), sodium sulfide ( $\text{Na}_2\text{S}\cdot 9\text{H}_2\text{O}$ ), and acetic acid ( $\text{HAc}$ ) were purchased with the highest quality via commercially available chemicals in the department.

**Synthesis of CdS@CTS.** CdS@CTS QDs were synthesized via mild hydrothermal conditions followed by a freeze-drying procedure. The chitosan solution was prepared via dissolving chitosan (0.1 g) in  $\text{H}_2\text{O}$  (20 mL) containing acetic acid (1 wt %).  $\text{Cd}(\text{NO}_3)_2$  (11 mg) was added to the chitosan solution. The solution was subjected to continuous stirring for 24 h to ensure the coordination between  $\text{Cd}^{2+}$  ions and the functional groups of CTS. A fresh solution of  $\text{Na}_2\text{S}$  (12 mg, 10 mL  $\text{H}_2\text{O}$ ) was added dropwise. A solution of  $\text{NH}_4\text{OH}$  (40 wt %) was added to obtain the solution's pH of 10. The solution was stirred at 90 °C until all excess ammonia was evaporated from the solution before freeze-drying.

**Characterization.** The X-ray diffraction (XRD) patterns were performed on a Philips PW1700 diffractometer (Philips, Netherlands, Cu  $K_\alpha$ , operating voltage 40 kV, and current of 40 mA). The size of quantum dots ( $D$ ) of the nanocrystal was calculated via Scherrer's formula, 1:

$$D = \frac{0.9\lambda}{\beta \cos \theta} \quad (1)$$

where  $\beta$ ,  $\lambda$ , and  $\theta$  are the diffraction angular width, the wavelength ( $\lambda$ ) = 1.5406 Å, and the diffraction angle, respectively.

The crystallinity index (CrI) of CTS before and after coordination with  $\text{Cd}^{2+}$  ions are determined using eq 2 as follows:

$$\text{CrI}_{110} = \frac{I_{110} - I_{\text{am}}}{I_{\text{am}}} \times 100 \quad (2)$$

$I_{110}$  is the maximum intensity of the crystalline peak from the (110) lattice diffraction, and  $I_{\text{am}}$  is the intensity of amorphous diffraction at  $2\theta = 10.4^\circ$ .

The transmission electron microscope (TEM) images, HR-TEM images, STEM images, and energy-dispersive X-ray (EDX) analysis/mapping were captured using JSM-2100 (JEOL, Japan). FT-IR spectra were taken using a Nicolet model 6700 spectrophotometer (Thermo Fisher, USA). X-ray photoelectron spectroscopy (XPS) spectra of CdS@CTS and Cu-CdS@CTS were recorded using a Thermo Fisher (K-alpha, Al  $K_\alpha$  radiation). The thermogravimetric analysis curves (TGA, PerkinElmer TGA T60) of CTS, Cd@CTS, CdS@CTS, and Cu-CdS@CTS were carried out under an air atmosphere. The UV–visible absorption spectrum of the CdS@CTS composite was recorded using a UV–vis spectrophotometer (Cary Eclipse, Agilent). The particle size was determined via the UV–vis spectrum using the empirical equation (eq 3).<sup>59</sup>

$$D = (9.8127 \times 10^{-7}) \times \lambda_{\text{exc}}^3 - (1.7147 \times 10^{-3}) \times \lambda_{\text{exc}}^2 + (1.0064) \times \lambda_{\text{exc}} - (194.84) \quad (3)$$

$D$  (nm) and  $\lambda_{\text{exc}}$  (nm) are the particle size and wavelength of the first excitonic absorption peak.

The optical band gap was calculated using Tauc's plot (eq 4).

$$E(\text{eV}) = (\alpha h\nu)^2 = h\nu \quad (4)$$

The energy ( $E$ ) in eV was calculated using eq 5.

$$E(\text{eV}) = \frac{1240}{\lambda(\text{nm})} \quad (5)$$

$\lambda$  is the absorbance wavelength in nm.

Nitrogen adsorption–desorption for CdS@CTS was carried out using Quantachrom (Model Nova 3200, USA) at  $-196\text{ }^\circ\text{C}$  using liquid nitrogen ( $\text{N}_2$ ). CdS@CTS powder was degassed at  $110\text{ }^\circ\text{C}$ . The pore size distribution analysis was evaluated using Barrett–Joyner–Halenda (BJH), density functional theory (DFT), and Dollimore–Heal (DH). UV–vis diffuse reflectance spectroscopy (DRS) for CdS, metal salts ( $\text{CoCl}_2$ ,  $\text{Ni}(\text{NO}_3)_2$ , and  $\text{CuSO}_4$ ), and CdS@CTS before and after interactions with these metal salts were evaluated using the Evolution 220 spectrophotometer (Thermo Fisher Scientific, UK).

**Metal Ion Interactions.** A stock solution of CdS@CTS was prepared using a 1 mg/mL concentration. The metal ions solutions were prepared by dissolving the corresponding metal salts in distilled water with a concentration of 1000 ppm.

The metal ions interaction for different metal ions was measured using 1 mL of each metal solution to a solution of CdS@CTS. The solution of  $\text{Cu}^{2+}$  ions (10–300  $\mu\text{L}$ ) was added to 1 mL of CdS@CTS. The UV–Vis absorption was measured for the prepared solution after 10 min.

## RESULTS AND DISCUSSION

**Materials Synthesis and Characterization.** The schematic representation for the synthesis of CdS@CTS is shown in Figure 1. Cadmium ( $\text{Cd}^{2+}$ ) ions are stirred with CTS for 24 h to ensure the coordination between  $\text{Cd}^{2+}$  ions and the functional groups of CTS, i.e.,  $-\text{OH}$  and  $-\text{NH}_2$  (Figure 1). The  $\text{S}^{2-}$  ions have a molecular volume of about  $25\text{ \AA}^3$ ; thus, they can penetrate easily into Cd-coordinated CTS to react with  $\text{Cd}^{2+}$  forming CdS@CTS (Figure 1). The formed material was then separated and dried via a freeze-drying method (Figure 1). The mechanism of the material formation was further supported using XRD (Figure 2a,b), FT-IR (Figure 2c), and TGA (Figure S1). The material CdS@CTS QDs were characterized using XRD (Figure 2a,b), XPS (Figure 3), TEM and HR-TEM images (Figure 4, Figures S2 and S3), STEM and EDX analysis/mapping (Figure 5), nitrogen adsorption–desorption isotherm (Figure 6, Figures S4 and S5), TGA (Figure S1), UV–vis spectroscopy (Figure 7a,b), and DRS (Figure 7c,d).

The XRD pattern of CTS showed peaks for Bragg's diffraction angle ( $2\theta$ ) at  $10.4$  and  $20.1^\circ$  corresponding to the Miller index of (020), and (110), respectively, representing their crystal lattice constant of  $8.470\text{ \AA}$  and  $4.075\text{ \AA}$ , respectively.<sup>60,61</sup> The diffraction peaks indicate the high degree of crystallinity of chitosan. The  $\text{CrI}_{110}$  is 62.8% for pure CTS. The Cd-coordinated CTS shows an insignificant change in the diffraction pattern of CTS, except for low crystallinity (Figure 2a). After the coordination of  $\text{Cd}^{2+}$  ions to the functional groups of CTS, the crystallinity is dropped significantly, making it difficult to determine  $\text{CrI}_{110}$  precisely. However, the crystallinity of CdS@CTS after the addition of  $\text{S}^{2-}$  is recovered. The  $\text{CrI}_{110}$  is 56.8% for Cd@CTS (Figure 2a). The XRD pattern of CdS@CTS shows peaks at Bragg's angles ( $2\theta$ ) =  $26.5^\circ$ ,  $30.6^\circ$ ,  $43.9^\circ$ ,  $51.9^\circ$ , and  $52.1^\circ$ , which can be indexed as (111), (102), (110), (220), and (311) planes, respectively, for the hexagonal phase CdS (JCPDS 42-1411, Figure 2a). The major diffraction peaks correspond to the CdS phase that matched the simulated XRD pattern for CdS revealing the successful formation of a hexagonal phase of CdS

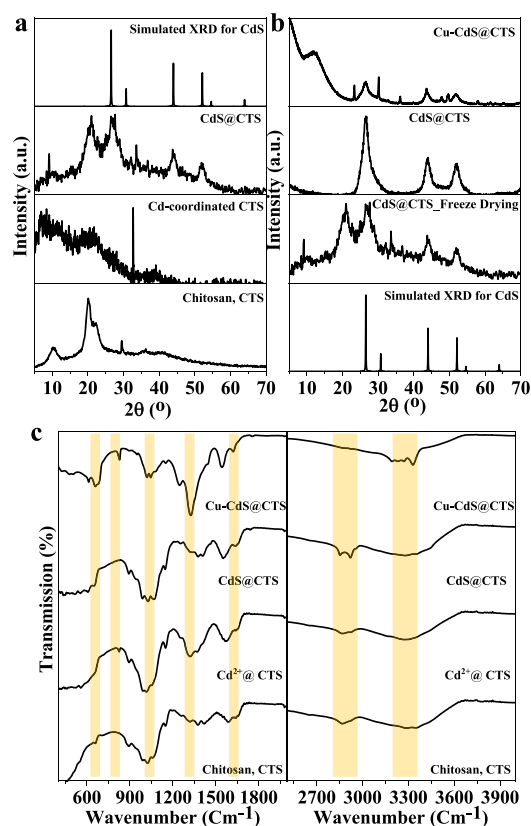


**Figure 2.** (a,b) XRD patterns for (a) CTS before and after coordinating with  $\text{Cd}^{2+}$  ions and formation of CdS@CTS and (b) CdS@CTS with and without freeze-drying and after interaction with  $\text{Cu}^{2+}$  ions for CdS@CTS\_Freeze drying, and (c) FT-IR spectra of CTS,  $\text{Cd}^{2+}$ @CTS, CdS@CTS, and Cu\_CdS@CTS.

on CTS via the in situ biomimetic synthesis method (Figure 1). According to Scherrer's equation, the average size of the crystallite CdS@CTS is approximately 3.7 nm (eq 1). The diffraction peaks' broadening is due to the small particle size of CdS QDs. The diffraction peaks of CTS are still present in the final product of CdS@CTS compared to CdS@CTS synthesized without freeze-drying (Figure 2b). No extra peaks except for CdS are observed in Figure 2b. This observation indicates that drying CdS@CTS via freeze-drying maintains the crystallinity of CTS in the final product, i.e., CdS@CTS compared to the same materials without the freeze-drying process (Figure 2b).<sup>54</sup>

Before and after coordination with  $\text{Cd}^{2+}$  ions, CTS was characterized using FT-IR spectra (Figure 2c). The vibrational peaks in the wavenumber range of  $3300\text{--}3450\text{ cm}^{-1}$  corresponding to the stretching vibrations for the functional groups of hydroxyl, amino, and amide groups showed shifts in the wavenumber's values (Table S1). The change in the wavenumber indicates the strong interaction between the functional groups of CTS and  $\text{Cd}^{2+}$  ions. The peaks at  $1256$  and  $1056\text{ cm}^{-1}$  are assigned to C–H and C3–O stretching, respectively (Table S1). The shift in N–H and O–H indicates that  $\text{Cd}^{2+}$  interacted via those functional groups of CTS (Figure 1). There is no dramatic change in the peak at  $1030\text{ cm}^{-1}$  attributed to C6–O stretching (Table S1). These changes indicate that N2 and O3 groups interact strongly with  $\text{Cd}^{2+}$  ions, while hydroxyl groups at C6 exhibit little contribution in these interactions. Based on these observations, we may infer that the possible spatial sites of  $\text{Cd}^{2+}$  and CdS

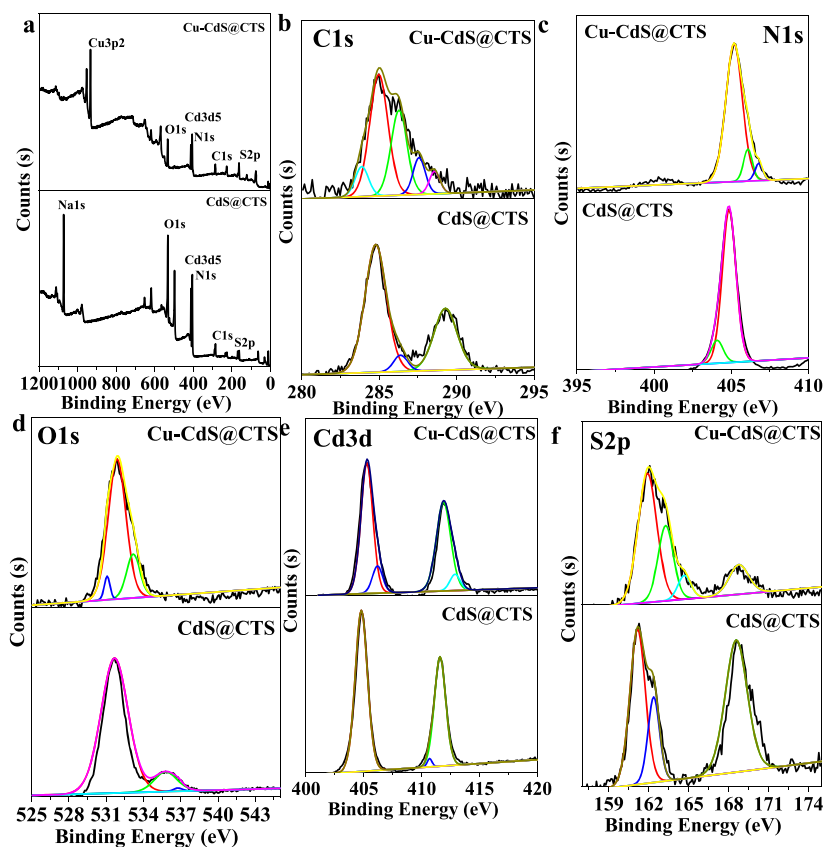


**Figure 3.** XPS analysis of CdS@CTS before and after interactions with Cu<sup>2+</sup> ions, (a) survey, (b) C 1s, (c) N 1s, (d) O 1s, (e) Cd3d<sub>5/2</sub>, and (f) S 2p.

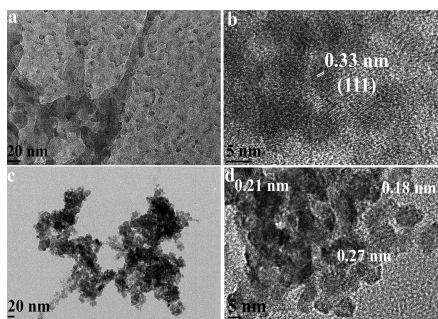


**Figure 4.** (a, c) TEM and (b, d) HR-TEM for (a, b) CdS@CTS and (c, d) Cu-CdS@CTS.

QDs are located near the C2 and C3 of the CTS units. FT-IR spectra revealed the formation of strong hydrogen bonding between the CdS QDs and CTS via N2 and O3 groups.<sup>62</sup>

The interactions within CdS@CTS were further characterized using XPS (Figure 3). XPS elemental survey shows elements of Cd 3d<sub>5/2</sub>, Na 1s, O 1s, S 2p, and C 1s binding energy (BE) of 409.1 eV, 1077.1 eV, 540.1 eV, 166.1 eV, and 288.1 eV, respectively (Figure 3a). N 1s is overlapped with Cd 3d<sub>5/2</sub>. However, the overlap between the N 1s and Cd 3d<sub>5/2</sub> regions can be resolved with peak fitting. Cl 2p at a binding energy of 202.1 eV indicates that Na 1s is due to ubiquitous salt, i.e., NaCl. The C 1s spectrum shows peaks at BEs of 284.8 eV, 286.4 eV, and 289.2 eV, referring to C–C, C–O–C, and C(N)–C=O, respectively (Figure 3b). N 1s spectrum shows peaks at BEs of 404.7 eV and 404.0 eV (Figure 3c). The analysis of O 1s shows peaks at BEs of 531.6 eV, 535.8 eV, and

536.6 eV corresponding to C–O, C=O, and Na KLL Auger, respectively (Figure 3d). The XPS spectrum for Cd 3d<sub>5/2</sub> shows peaks at 404.8 eV and 411.5 eV corresponding to Cd 3d<sub>5/2</sub> and Cd 3d<sub>3/2</sub>, respectively (Figure 3e). The analysis of Cd 3d confirms the presence of CdS. The small peak at a binding energy of 410.7 eV is due to the interaction of CdS and the functional groups of CTS (Figure 3e). The S 2p shows peaks at 161.1 eV and 162.4 eV assigned to S 2p<sub>3/2</sub> and S 2p<sub>1/2</sub>, respectively (Figure 3f). The peak at the BE of 168.5 eV is due to the oxidized S, i.e., SO<sub>3</sub><sup>2-</sup> or SO<sub>4</sub><sup>2-</sup> on the external surface of CdS (Figure 3f). XPS analysis confirms the successful formation of CdS@CTS with the interaction between the CdS core and the functional groups of CTS (Figure 3).

TEM and HR-TEM images confirm the presence of nanocrystals with a particle size of 1–7 nm with clear lattice fringes due to high crystallinity (Figure 4). TEM images show a uniform distribution of CdS inside chitosan. The particle size distribution is shown in Figures S2 and S3, indicating a particle size of 1–7 nm with an average particle size of 2.6 nm. The HR-TEM image of CdS@CTS shows lattice fringes with an interplanar distance of 0.33 nm corresponding to the Miller index plane (111) (Figure 2a).

STEM image indicates the homogenous distribution of CdS QDs inside CTS (Figure 5a). The distribution of CdS inside CTS was further confirmed using EDX analysis and mapping (Figure 5). The elemental analysis using EDX analysis confirms the presence of elements C, N, O, Cd, and S (Figure 5b). The elemental distribution of observed elements indicates that Cd is mainly present near CTS functional groups such as NH and OH (Figure 5c–h). This observation confirms the

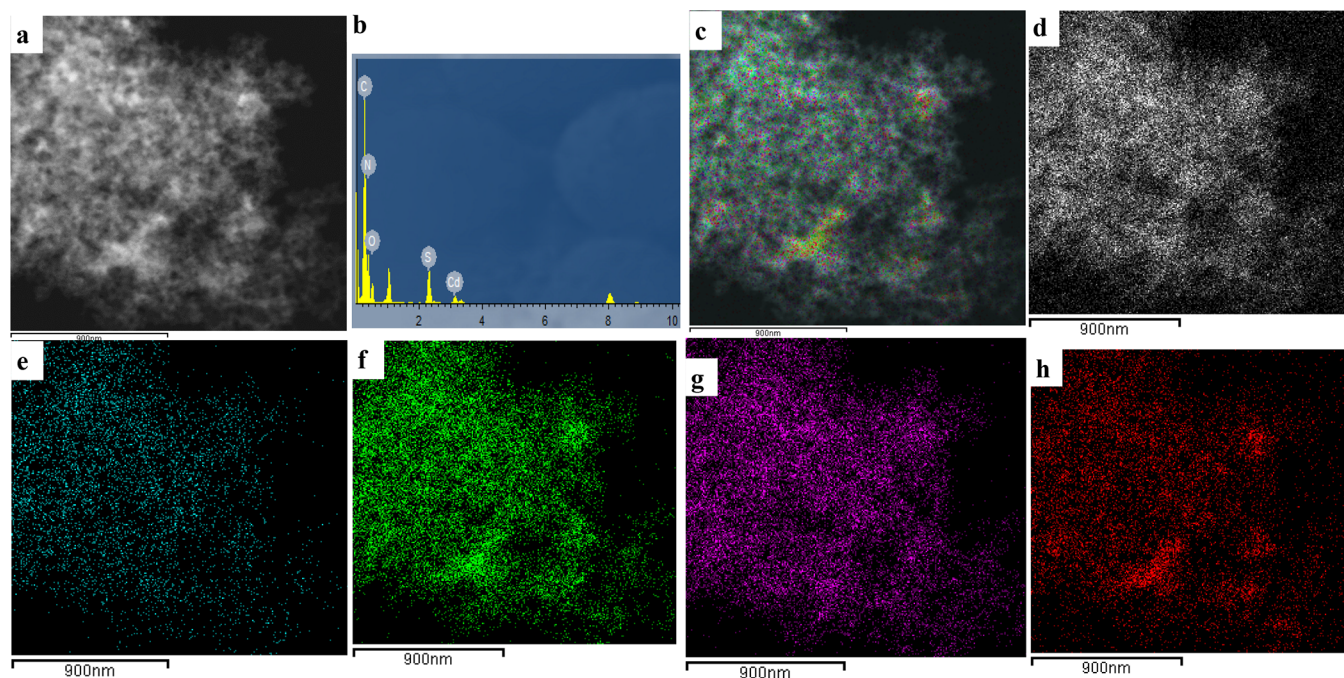


**Figure 5.** (a) STEM image, (b) EDX analysis, and (c–h) EDX mapping of elements (c) merged colored, (d) C, (e) Cd, (f) S, (g) N, and (h) O.

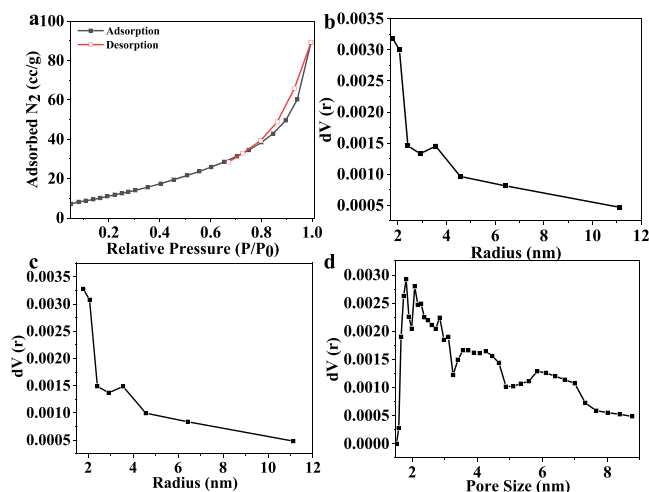


**Figure 6.** (a) Nitrogen adsorption–desorption isotherm, (b–d) pore size distribution using (b) BJH, (c) HK, and (d) DFT.

results of the XRD, XPS, and HR-TEM images. It also approves that CdS and CTS are a composite, i.e., no mixture.

The surface area and pore size distribution of CdS@CTS were characterized using a nitrogen adsorption–desorption isotherm (Figure 6, Figures S4 and S5). The specific surface area and external surface area are evaluated using Brunauer–Emmett–Teller (BET, Figure S3) and the t-plot method (BET, Figure S4). Data show BET and an external specific surface area of 50 m<sup>2</sup>/g. The pore size distribution in CdS@CTS is evaluated using the BJH method (Figure 6b), DH (Figure 6c), and DFT (Figure 6d). Data analysis indicates the presence of a pore size of 1.8–11 nm (Figure 6b,d). The porosity of CdS@CTS is created due to the interparticle between CdS and CTS. The material's porosity is improved using freeze-drying.

Thermal analysis of CTS, Cd@CTS, and CdS@CTS is evaluated using TGA (Figure S1). TGA thermograms of CTS

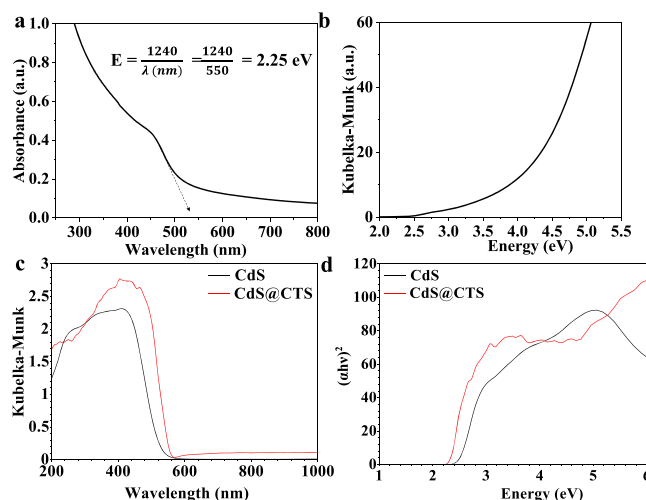


**Figure 7.** (a–c) UV–vis spectroscopy and (b–d) Tauc's plot for (a, b) solution and (c, d) solid samples.

show gradual weight loss due to their organic nature, reaching complete decomposition at 545 °C (Figure S1). Cd-coordinated CTS offers higher thermal stability with a metal residual of 5 wt %. The presence of Cd<sup>2+</sup> ions in the CTS improved the thermal stability of CTS. CdS QDs exhibit further improvement in the thermal stability of CTS. The thermal decomposition of CTS was shifted toward a higher temperature by about 60 °C after conjugation with CdS QDs.<sup>62</sup> The TGA thermogram of CdS@CTS shows three stages of weight loss: (1) about 13% weight loss from room temperature to 234 °C; (2) 44% weight loss from 250 °C to 464 °C; and (3) 38% weight loss from 464 °C to 526 °C. The first weight-loss stage referred to the evaporation of physically adsorbed molecules such as water. The other weight loss steps are due to the chemisorbed water and residual organics in CdS@CTS. TGA analysis indicates that Cd-coordinated CTS

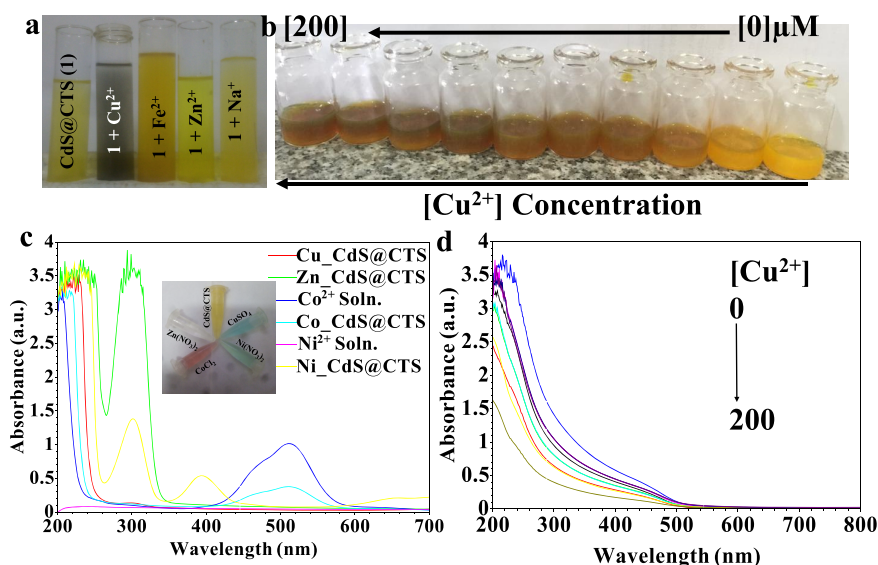


**Figure 8.** (a, b) color change of CdS@CTS QDs upon interaction with (a) heavy metal ions, and (b) different concentration of  $\text{Cu}^{2+}$  ions. (c, d) UV-vis spectra of CdS@CTS QDs upon interaction with (c) different heavy metals; inset camera image show the solution of CdS@CTS and some solution of the tested metal salts, different concentrations of  $\text{Cu}^{2+}$  ions, and (d) different concentrations of  $\text{Cu}^{2+}$  ions.

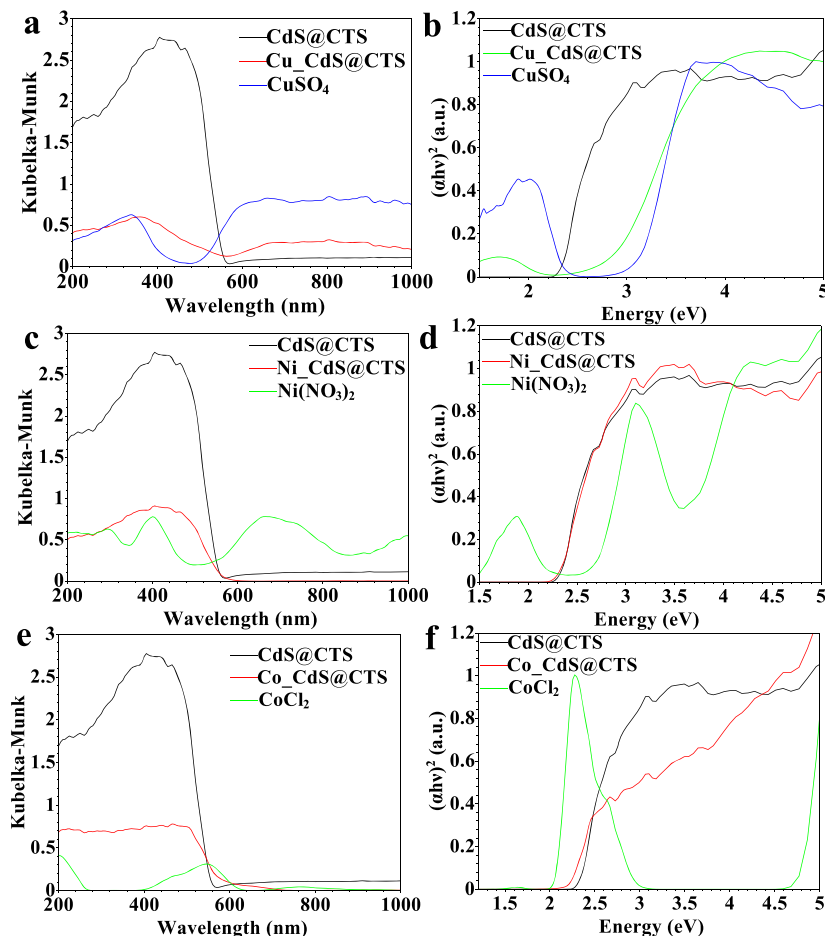


**Figure 9.** (a, c, e) DRS spectra and (b, d, f) Tauc's plots of CdS@CTS before and after interactions with (a, b)  $\text{Cu}^{2+}$ , (c, d)  $\text{Ni}^{2+}$ , and (e, f)  $\text{Co}^{2+}$  ions and their corresponding salts.

and CdS@CTS composite exhibited higher thermal stability than the pure CTS (Figure S1).

**Optical Properties of CdS@CTS.** The optical properties of CdS@CTS were evaluated using UV-vis spectroscopy

(Figure 7a,b) and DRS (Figure 7c,d). The UV-vis spectrum of CdS@CTS was recorded, as shown in Figure 7. The UV-vis spectrum of the CdS@CTS QDs shows a shoulder absorption onset at 550 nm (Figure 7a). Based on the

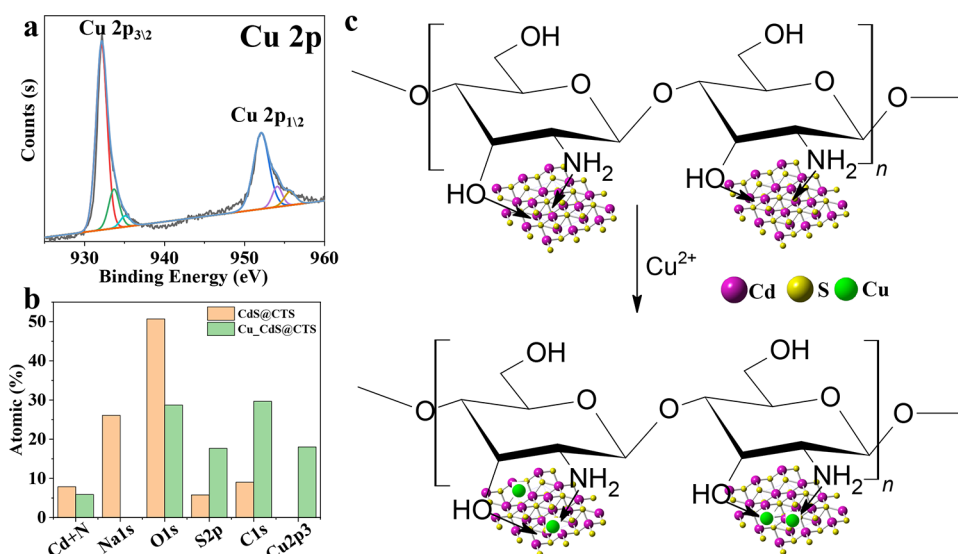


**Figure 10.** (a) XPS for Cu 2p, (b) XPS for quantitative elemental analysis, and (c) mechanism of the formation of Cu\_CdS@CTS.

empirical equation (eq 2), the CdS@CTS nanocrystals have an average particle size of 3.1 nm, which agrees with the particle size range obtained from TEM and HR-TEM (Figure 4). The Kubelka–Munk plot for CdS@CTS using Tauc's equation is plotted as  $(ah\nu)^2$  versus  $h\nu$  (Figure 7b). The band gap energy ( $E_g$ ) value for CdS@CTS is 2.25 eV (Figure 7b). The optical properties of CdS with and without CTS were evaluated using DRS (Figure 7c,d). DRS spectra of CdS and CdS@CTS show absorbance in the range of 200–570 nm (Figure 7c,d). There are apparent differences in the case of CdS@CTS compared to bare CdS. The difference in the DRS is due to the interaction between CdS and CTS's functional groups. Tauc's plot of CdS and CdS@CTS indicates an optical band gap of 2.47 and 2.30 eV, respectively (Figure 7c,d). CTS decreases the optical band gap for the core of CdS.

**Mechanism of Interactions.** CdS@CTS QDs exhibit good photophysical properties. Thus, they can be used to detect heavy metal ions. The dispersed solution of CdS@CTS QDs shows a yellow color (Figure 8a). The color of CdS@CTS QDs after adding metal ions such as Cu<sup>2+</sup>, Ca<sup>2+</sup>, Zn<sup>2+</sup>, Mg<sup>2+</sup>, Ni<sup>2+</sup>, Fe<sup>2+</sup>, Co<sup>2+</sup>, Na<sup>+</sup>, and K<sup>+</sup> was evaluated in Figure 8a. Except for Cu<sup>2+</sup>, there are insignificant changes in the solution's color of CdS@CTS QDs (Figure 8a). The change in the yellow color of CdS@CTS QDs upon interaction with Cu<sup>2+</sup> ions indicates the potential of our probe to detect Cu<sup>2+</sup> ions using naked eyes (Figure 8b). These observations suggest the high selectivity of CdS@CTS QDs toward Cu<sup>2+</sup> ions compared to other metal ions (Figure 8c). The absorption peak of the colored metal salts is also observed (Figure 8c). The change in the optical properties of CdS@CTS upon interaction with different can be recorded using UV–vis spectroscopy (Figure 8d). The color change upon interaction with Cu<sup>2+</sup> ions is speedy and can occur after the complete addition of the solution of Cu<sup>2+</sup> ion (see Movie S1).

The optical properties of CdS@CTS before and after interaction with color metal salts, i.e., Ni<sup>2+</sup>, Co<sup>2+</sup>, and Cu<sup>2+</sup>, are evaluated using DRS (Figure 9) of CdS@CTS that was shifted to 3.2 eV, indicating the strong interaction of the CdS and Cu<sup>2+</sup> ions (Figure 9). This observation can be confirmed by the color change in the solution of CdS@CTS. Other metal ions such as Co<sup>2+</sup> and Ni<sup>2+</sup> show minimal change indicating

that they can only interact with the functional groups of CTS. Thus, we can claim that CdS@CTS shows selective interaction with Cu<sup>2+</sup> ions.

The mechanism of interactions between CdS@CTS QDs and Cu<sup>2+</sup> ions has been investigated using XRD (Figure 2b), FT-IR (Figure 2c), XPS (Figure 3, Figure 12), TEM, and HR-TEM images (Figure 4c,d), STEM, and EDX analysis/mapping (Figure 13). The XRD pattern of CdS@CTS QDs after interaction with Cu<sup>2+</sup> ions shows the prominent diffraction peaks of pure CdS@CTS QDs (Figure 2b). Furthermore, extra peaks at Bragg's diffraction angles were also observed corresponding to the diffraction peaks of CuS (JCPDS no. 79–2321, Figure 2b). This observation indicates that Cu<sup>2+</sup> replaces Cd<sup>2+</sup> in CdS@CTS QDs (i.e., formation of Cu\_CdS@CTS) or coordinates to the functional groups of CTS. There is no dramatic change in the particle size of CdS@CTS after interaction with Cu<sup>2+</sup> ions. TEM and HR-TEM images show aggregation of quantum dots with particle sizes less than 10 nm (Figure 4c,d).

The changes in the functional groups of CTS for CdS@CTS QDs upon interactions with Cu<sup>2+</sup> ions (i.e., Cu\_CdS@CTS) are characterized using FT-IR spectroscopy (Figure 2c). Like the XRD pattern, the FT-IR spectrum for Cu\_CdS@CTS displays the main functional groups of pure CdS@CTS with an insignificant shift in the vibrational wavenumber (Table S1). Moreover, extra peaks at wavenumbers of 1331 and 655 cm<sup>-1</sup> can be assigned corresponding to Cu–S. Several studies reported the high affinity of metal ions toward CTS's functional groups, i.e., N–H and O–H. An adsorption study reported that the metal ions of different cations could be adsorbed on a CTS film following the order of Cu<sup>2+</sup> >> Hg<sup>2+</sup> > Zn<sup>2+</sup> > Cd<sup>2+</sup> > Ni<sup>2+</sup> > Co<sup>2+</sup> ions.<sup>63</sup> This observation could explain the high selectivity of CdS@CTS QDs toward Cu<sup>2+</sup> ions.

The XPS analysis of Cu\_CdS@CTS is shown in Figure 3. The data analysis of CdS@CTS before and after interaction with Cu<sup>2+</sup> ions indicates significant changes in the peak fitting. The analysis of the C 1s spectrum shows peaks at binding energies of 283.8 eV, 284.9 eV, 286.3 eV, 287.6 eV, and 288.6 eV (Figure 3b). The peaks at binding energies of 283.8 eV, 286.3 eV, and 288.6 eV correspond to C–C, C–O–C, and

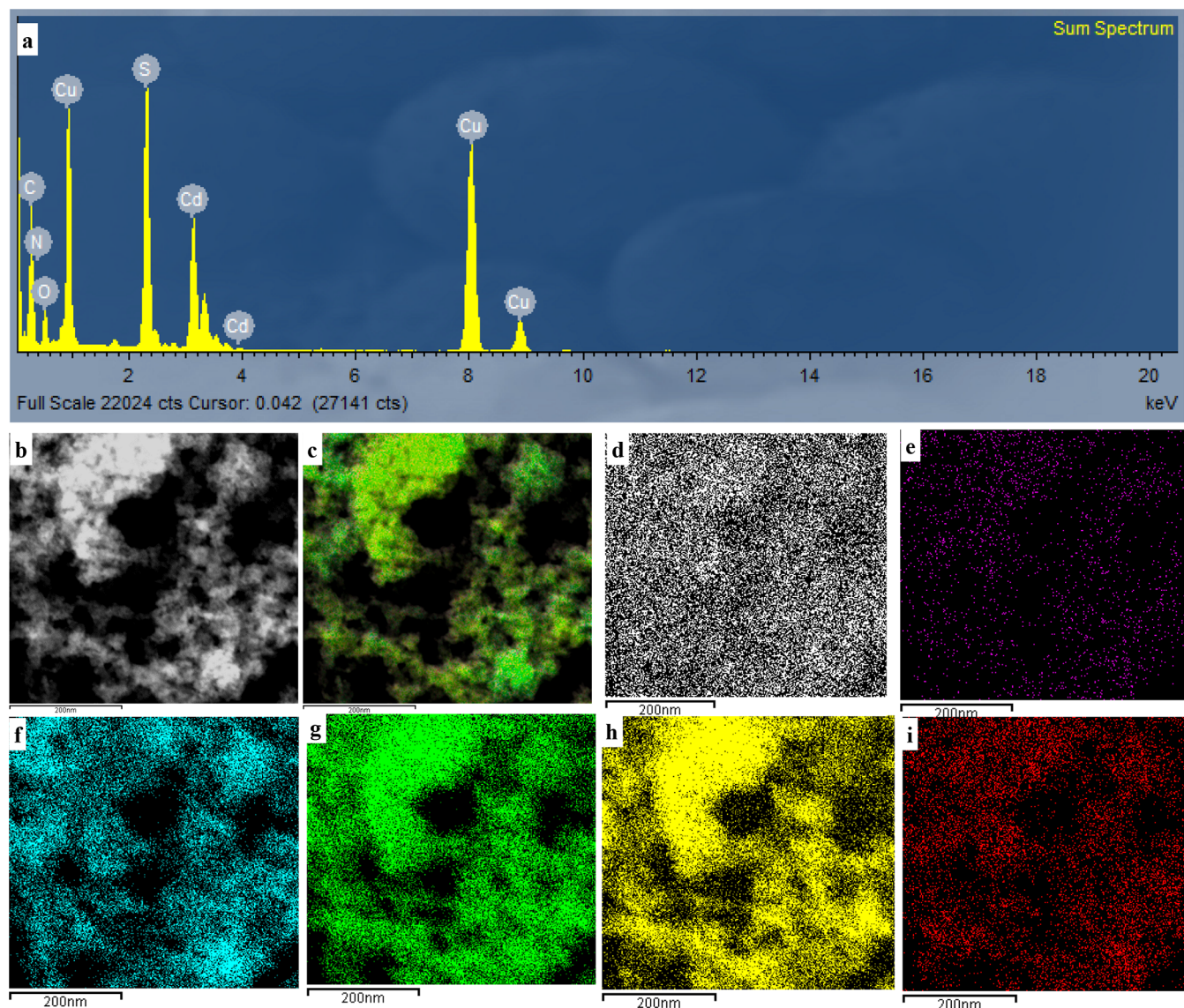


**Figure 11.** (a) EDX analysis, (b) STEM image, and (c–h) EDX mapping of elements; (c) merged colored, (d) C, (e) N, (f) Cd, (g) S, (h) Cu, and (i) O.

C(N)—C=O, respectively (Figure 3b). The extra peaks are due to the interactions with  $\text{Cu}^{2+}$  ions that confirm the interaction between  $\text{Cu}^{2+}$  ions and the functional groups of CTS, i.e., O—H and N—H. The N 1s spectrum shows peaks at 405.2 eV, 406.1 eV, and 406.8 eV. No depth conclusion can be taken from the analysis of N 1s, even the significant change in the data fitting, due to the overlap between N 1s and Cd 3d. The analysis of the O 1s spectrum shows a peak at 531.0 eV, 531.9 eV, and 533.2 eV corresponding to C—O  $\rightarrow$  Cd, C—O  $\rightarrow$  Cu, and C=O, respectively (Figure 3d). Cd 3d<sub>5/2</sub> shows peaks at 405.3 eV, 406.2 eV, 411.8 eV, and 412.8 eV. Cd 3d<sub>3/2</sub> shows peaks at 405.3 eV and 412.8 eV corresponding to Cd 3d<sub>5/2</sub> and Cd 3d<sub>3/2</sub> (Figure 3e). The analysis of S 2p shows a peak at binding energies of 161.9 eV and 163.3 eV corresponding to S 2p<sub>3/2</sub> and S 2p<sub>1/2</sub>, respectively (Figure 3f). The new peak at 164.6 eV is due to Cu—S. The peak at 168.8 eV is due to  $\text{SO}_3^{2-}$  or  $\text{SO}_4^{2-}$  coming from the oxidation of  $\text{S}^{2-}$  on the external surface of CdS. This peak is low in the presence of Cu, indicating that  $\text{Cu}^{2+}$  prevents further oxidation of sulfide on the external surface of CdS. There are significant

peak shifts in XPS spectra indicating the replacement of  $\text{Cd}^{2+}$  with  $\text{Cu}^{2+}$  and the formation of  $\text{CuS@CTS}$ .

The presence of Cu in the final product, i.e.,  $\text{Cu}_x\text{CdS}@CTS$ , can be confirmed from the XPS spectrum (Figure 10a).<sup>64</sup> XPS analysis shows a peak at a binding energy of 933.2 eV corresponding to Cu 2p (Figure 10a). The XPS spectrum of Cu 2p shows peaks at binding energies of 932.2 eV and 952.1 eV corresponding to Cu 2p<sub>3/2</sub> and Cu 2p<sub>1/2</sub>, respectively. We could not observe satellite peaks reported for CuO, indicating that the present form of Cu is pure CuS.<sup>65</sup> The peaks fitting Cu 2p<sub>3/2</sub> show three peaks at 932.2 eV, 933.8 eV, and 935.1 eV corresponding to Cu—S, Cu—O, and Cu—N, respectively. The chemical analysis of the elements in  $\text{CdS@CTS}$  and  $\text{Cu}_x\text{CdS}@CTS$  is shown in Figure 10b. The presence of  $\text{Na}^+$  ions in  $\text{CdS@CTS}$  is due to the ion mineralization of CTS. This makes direct quantitative analysis a tedious task.

Furthermore, there is an overlap between N 1s and Cd 3d. However, the quantitative analysis ensures the presence of a high concentration of Cu in  $\text{Cu}_x\text{CdS}@CTS$  due to the replacement with Cd in CdS and the coordination with the

functional groups of CTS (Figure 10c). The mechanism can be explained due to the strong binding of  $\text{Cu}^{2+}$  onto the surface of CdS and the functional groups of CTS, resulting in the formation of CuS on the external surface of the CdS QDs.<sup>66</sup>

The elemental analysis and mapping for Cu\_CdS@CTS are characterized further using EDX analysis and mapping (Figure 11). EDX analysis (Figure 11a) confirms the presence of Cu, Cd, and S in Cu\_CdS@CTS, which agrees with XPS analysis data (Figure 10a). The elemental mapping of C, N, S, Cd, and Cu ensures the well dispersion of Cu\_CdS inside CTS (Figure 11c–i). STEM images indicate the homogenous distribution of Cu\_CdS inside CTS frameworks (Figure 11b).

Chitosan offers several advantages of being a suitable biopolymer to synthesize CdS-based QDs. It formed complexes with  $\text{Cd}^{2+}$  ions via coordination during the in situ growth of CdS QDs. Chitosan's functional groups, such as amino and hydroxyl, serve as influential capping functional groups for CdS QDs. The viscosity of CTS solution during the in situ growth of CdS prevents the aggregation and agglomeration of QDs offering high dispersion of QDs into the CTS matrix. The functional groups of CTS can be selectively bound to  $\text{Cu}^{2+}$  ions offering selective sensing compared to other heavy metal ions. CTS plays several roles; (1) modulator during the in situ growth of CdS QDs; (2) stabilizer for CdS; and chelator for heavy metal ions with high selectivity toward  $\text{Cu}^{2+}$  ions. The prepared materials, i.e., CdS@CTS or Cu\_CdS@CTS, seem promising for further biosensing, photocatalysis, and energy-based applications.

## CONCLUSIONS

A facile synthesis procedure was reported to synthesize homogenous dispersed CdS QDs inside CTS. It requires mild synthesis conditions and is a one-pot synthesis procedure. The functional groups of biopolymer chitosan CTS were potential matrices to grow CdS QDs via an in situ approach with a narrow size distribution (1–7 nm). The synthesized CdS@CTS exhibits good photophysical properties. Heavy metal ions (Cd after coordination, formation of CdS, and Cu after adsorption into CdS@CTS) improved the thermal properties of pure CTS. CdS@CTS can selectively interact with  $\text{Cu}^{2+}$  ions offering naked-eye detection. The data analysis provides a comprehensive, in-depth discussion of the interaction between heavy metal ions and CdS@CTS QDs. Our results may open new avenues for the material chemistry of quantum dots and advance the biosensing and analytical chemistry toward metal ion detection/sensing.

## ASSOCIATED CONTENT

### Supporting Information

The Supporting Information is available free of charge at <https://pubs.acs.org/doi/10.1021/acsomega.2c01793>.

TGA curves, TEM images, particle distribution, the linear plot for BET specific surface area, and peak assignments in FT-IR spectra of chitosan and CdS@CTS (PDF)

Color change upon interaction with  $\text{Cu}^{2+}$  ions after the addition of the of  $\text{Cu}^{2+}$  ion solution (MP4)

## AUTHOR INFORMATION

### Corresponding Authors

Faisal K. Algethami – Department of Chemistry, College of Science, Imam Mohammad Ibn Saud Islamic University

(IMSIU), Riyadh 11432, Saudi Arabia;

Email: [falgethami@imamu.edu.sa](mailto:falgethami@imamu.edu.sa)

Hani Nasser Abdelhamid – Department of Chemistry, Advanced Multifunctional Materials Laboratory, Faculty of Science, Assiut University, Assiut 71575, Egypt; Nanotechnology Research Centre (NTRC), The British University in Egypt (BUE), El-Sherouk City, Cairo 11837, Egypt; [orcid.org/0000-0002-3106-8302](https://orcid.org/0000-0002-3106-8302); Email: [abdelhamid@aun.edu.eg](mailto:abdelhamid@aun.edu.eg)

## Authors

Ilyes Saidi – Laboratory of Heterocyclic Chemistry, Natural Products and Reactivity (LR11ES39), Medicinal Chemistry and Natural Products Team, Faculty of Science of Monastir, University of Monastir, Avenue of Environment, Monastir 5019, Tunisia

Hichem Ben Jannet – Laboratory of Heterocyclic Chemistry, Natural Products and Reactivity (LR11ES39), Medicinal Chemistry and Natural Products Team, Faculty of Science of Monastir, University of Monastir, Avenue of Environment, Monastir 5019, Tunisia

M. Khairy – Department of Chemistry, College of Science, Imam Mohammad Ibn Saud Islamic University (IMSIU), Riyadh 11432, Saudi Arabia

Babiker Y. Abdulkhair – Department of Chemistry, College of Science, Imam Mohammad Ibn Saud Islamic University (IMSIU), Riyadh 11432, Saudi Arabia

Youssef O. Al-Ghamdi – Department of Chemistry, College of Science Al-zulfi, Majmaah University, Al-Majmaah 11952, Saudi Arabia

Complete contact information is available at:

<https://pubs.acs.org/10.1021/acsomega.2c01793>

## Notes

The authors declare no competing financial interest.

## ACKNOWLEDGMENTS

The authors extend their appreciation to the Deanship of Scientific Research at Imam Mohammad Ibn Saud Islamic University for funding this work through research group no. RG-21-09-69.

## REFERENCES

- (1) Abdelhamid, H. N.; Mathew, A. P. Cellulose-Metal Organic Frameworks (CelloMOFs) Hybrid Materials and Their Multifaceted Applications: A Review. *Coord. Chem. Rev.* **2022**, *451*, No. 214263.
- (2) Abdelhamid, H. N.; Mathew, A. P. A Review on Cellulose-Based Materials for Biomedicine. *Preprints* **2022**, 2022010035. [ht10.20944/preprints202201.0035.v1](https://doi.org/10.20944/preprints202201.0035.v1).
- (3) Nasser Abdelhamid, H.; Mathew, A. P. Cellulose-Zeolitic Imidazolate Frameworks (CelloZIFs) for Multifunctional Environmental Remediation: Adsorption and Catalytic Degradation. *Chem. Eng. J.* **2021**, *426*, 131733.
- (4) Abdelhamid, H. N.; Mathew, A. P. Cellulose-Based Materials for Water Remediation: Adsorption, Catalysis, and Antifouling. *Front. Chem. Eng.* **2021**, *3*, No. 790314.
- (5) Abdelhamid, H. N.; Mathew, A. P. In-Situ Growth of Zeolitic Imidazolate Frameworks into a Cellulosic Filter Paper for the Reduction of 4-Nitrophenol. *Carbohydr. Polym.* **2021**, *274*, No. 118657.
- (6) Saheed, I. O.; Da Oh, W.; Suah, F. B. M. Chitosan Modifications for Adsorption of Pollutants – A Review. *J. Hazard. Mater.* **2021**, *408*, No. 124889.
- (7) Ahmad, S. I.; Ahmad, R.; Khan, M. S.; Kant, R.; Shahid, S.; Gautam, L.; Hasan, G. M.; Hassan, M. I. Chitin and Its Derivatives:

- Structural Properties and Biomedical Applications. *Int. J. Biol. Macromol.* **2020**, *164*, 526–539.
- (8) Kou, S.; Peters, L. M.; Mucalo, M. R. Chitosan: A Review of Sources and Preparation Methods. *Int. J. Biol. Macromol.* **2021**, *169*, 85–94.
- (9) Negm, N. A.; Hefni, H. H. H.; Abd-Elal, A. A. A.; Badr, E. A.; Abou Kana, M. T. H. Advancement on Modification of Chitosan Biopolymer and Its Potential Applications. *Int. J. Biol. Macromol.* **2020**, *152*, 681–702.
- (10) Li, J.; Zhuang, S. Antibacterial Activity of Chitosan and Its Derivatives and Their Interaction Mechanism with Bacteria: Current State and Perspectives. *Eur. Polym. J.* **2020**, *138*, No. 109984.
- (11) Kumar, A.; Sharma, G.; Naushad, M.; Ala'a, H.; Garcia-Peñas, A.; Mola, G. T.; Si, C.; Stadler, F. J. Bio-Inspired and Biomaterials-Based Hybrid Photocatalysts for Environmental Detoxification: A Review. *Chem. Eng. J.* **2020**, *382*, No. 122937.
- (12) Dowaidar, M.; Nasser Abdelhamid, H.; Hällbrink, M.; Langel, Ü.; Zou, X. Chitosan Enhances Gene Delivery of Oligonucleotide Complexes with Magnetic Nanoparticles–Cell-Penetrating Peptide. *J. Biomater. Appl.* **2018**, *33*, 392–401.
- (13) Abdelhamid, H. N.; Lin, Y. C.; Wu, H.-F. Magnetic Nanoparticle Modified Chitosan for Surface Enhanced Laser Desorption/Ionization Mass Spectrometry of Surfactants. *RSC Adv.* **2017**, *7*, 41585–41592.
- (14) Gopal, J.; Abdelhamid, H. N.; Hua, P.-Y.; Wu, H.-F. Chitosan Nanomagnets for Effective Extraction and Sensitive Mass Spectrometric Detection of Pathogenic Bacterial Endotoxin from Human Urine. *J. Mater. Chem. B* **2013**, *1*, 2463.
- (15) Monsef, R.; Salavati-Niasari, M. Electrochemical Sensor Based on a Chitosan-Molybdenum Vanadate Nanocomposite for Detection of Hydroxychloroquine in Biological Samples. *J. Colloid Interface Sci.* **2022**, *613*, 1–14.
- (16) Abdelhamid, H. N.; Dowaidar, M.; Langel, Ü. Carbonized Chitosan Encapsulated Hierarchical Porous Zeolitic Imidazolate Frameworks Nanoparticles for Gene Delivery. *Microporous Mesoporous Mater.* **2020**, *302*, No. 110200.
- (17) Tong, X.; Zhang, J.; Chen, Q.; Liu, H. Zeolitic Imidazolate Framework-8/Graphene Oxide/Magnetic Chitosan Nanocomposites for Efficient Removal of Congo Red from Aqueous Solution. *New J. Chem.* **2021**, *45*, 19416–19424.
- (18) Dowaidar, M.; Abdelhamid, H. N.; Langel, Ü. Improvement of Transfection with PepFects Using Organic and Inorganic Materials. *Cell Penetrating Peptides* **2022**, 555–567.
- (19) Abdelhamid, H. N.; Wu, H.-F. Multifunctional Graphene Magnetic Nanosheet Decorated with Chitosan for Highly Sensitive Detection of Pathogenic Bacteria. *J. Mater. Chem. B* **2013**, *1*, 3950–3961.
- (20) Rashki, S.; Asgarpour, K.; Tarrahimofrad, H.; Hashemipour, M.; Ebrahimi, M. S.; Fathizadeh, H.; Khorshidi, A.; Khan, H.; Marzhooseyni, Z.; Salavati-Niasari, M.; Mirzaei, H. Chitosan-Based Nanoparticles against Bacterial Infections. *Carbohydr. Polym.* **2021**, *251*, No. 117108.
- (21) Upadhyay, U.; Sreedhar, I.; Singh, S. A.; Patel, C. M.; Anitha, K. L. Recent Advances in Heavy Metal Removal by Chitosan Based Adsorbents. *Carbohydr. Polym.* **2021**, *251*, No. 117000.
- (22) Pal, P.; Pal, A.; Nakashima, K.; Yadav, B. K. Applications of Chitosan in Environmental Remediation: A Review. *Chemosphere* **2021**, *266*, No. 128934.
- (23) Mallakpour, S.; Sirous, F.; Hussain, C. M. Current Achievements in 3D Bioprinting Technology of Chitosan and Its Hybrids. *New J. Chem.* **2021**, *45*, 10565–10576.
- (24) Algar, W. R.; Massey, M.; Rees, K.; Higgins, R.; Krause, K. D.; Darwish, G. H.; Peveler, W. J.; Xiao, Z.; Tsai, H.-Y.; Gupta, R.; Lix, K.; Tran, M. V.; Kim, H. Photoluminescent Nanoparticles for Chemical and Biological Analysis and Imaging. *Chem. Rev.* **2021**, *121*, 9243–9358.
- (25) Efros, A. L.; Brus, L. E. Nanocrystal Quantum Dots: From Discovery to Modern Development. *ACS Nano* **2021**, *15*, 6192–6210.
- (26) Ganguly, A.; Nath, S. S.; Choudhury, M. Enhanced Efficiency in Swift Heavy Ion Irradiated CdS Quantum Dots Sensitized Solar Cell. *IEEE Photon. Technol. Lett.* **2018**, *30*, 1735–1738.
- (27) Ganguly, A.; Nath, S. S.; Choudhury, M. Effect of Mn Doping on Multilayer PbS Quantum Dots Sensitized Solar Cell. *IEEE J. Photovoltaics* **2018**, *8*, 1656–1661.
- (28) Abdelhamid, H. N. Quantum Dots Hybrid Systems for Drug Delivery. In *Hybrid Nanomaterials for Drug Delivery*; Elsevier, 2022; pp. 323–338, DOI: 10.1016/B978-0-323-85754-3.00013-7.
- (29) Martynenko, I. V.; Litvin, A. P.; Purcell-Milton, F.; Baranov, A. V.; Fedorov, A. V.; Gun'ko, Y. K. Application of Semiconductor Quantum Dots in Bioimaging and Biosensing. *J. Mater. Chem. B* **2017**, *5*, 6701–6727.
- (30) Akbari, M.; Rahimi-Nasrabadi, M.; Eghbali-Arani, M.; Banafshe, H. R.; Ahmadi, F.; Ganjali, M. R. CdTe Quantum Dots Prepared Using Herbal Species and Microorganisms and Their Anti-Cancer, Drug Delivery and Antibacterial Applications; a Review. *Ceram. Int.* **2020**, *46*, 9979–9989.
- (31) Saikia, M.; Das, T.; Saikia, B. K. A Novel Rapid Synthesis of Highly Stable Silver Nanoparticle/Carbon Quantum Dot Nanocomposites Derived from Low-Grade Coal Feedstock. *New J. Chem.* **2021**, *46*, 309–321.
- (32) Kazemifard, N.; Ensafi, A. A.; Dehkordi, Z. S. A Review of the Incorporation of QDs and Imprinting Technology in Optical Sensors – Imprinting Methods and Sensing Responses. *New J. Chem.* **2021**, *45*, 10170–10198.
- (33) Cheng, Y.; Da Ling, S.; Geng, Y.; Wang, Y.; Xu, J. Microfluidic Synthesis of Quantum Dots and Their Applications in Bio-Sensing and Bio-Imaging. *Nanoscale Adv.* **2021**, *3*, 2180–2195.
- (34) Yang, E.; Zhang, Y.; Shen, Y. Quantum Dots for Electrochemiluminescence Bioanalysis - A Review. *Anal. Chim. Acta* **2022**, No. 339140.
- (35) Zhang, J.; Jin, J.; Wan, J.; Jiang, S.; Wu, Y.; Wang, W.; Gong, X.; Wang, H. Quantum Dots-Based Hydrogels for Sensing Applications. *Chem. Eng. J.* **2021**, *408*, No. 127351.
- (36) Sobiech, M.; Luliński, P.; Wiczorek, P. P.; Marć, M. Quantum and Carbon Dots Conjugated Molecularly Imprinted Polymers as Advanced Nanomaterials for Selective Recognition of Analytes in Environmental, Food and Biomedical Applications. *TrAC Trends Anal. Chem.* **2021**, *142*, No. 116306.
- (37) Gholami, T.; Salavati-Niasari, M.; Varshoy, S. Electrochemical Hydrogen Storage Capacity and Optical Properties of NiAl<sub>2</sub>O<sub>4</sub>/NiO Nanocomposite Synthesized by Green Method. *Int. J. Hydrogen Energy* **2017**, *42*, 5235–5245.
- (38) Panahi-Kalamuei, M.; Alizadeh, S.; Mousavi-Kamazani, M.; Salavati-Niasari, M. Synthesis and Characterization of CeO<sub>2</sub> Nanoparticles via Hydrothermal Route. *J. Ind. Eng. Chem.* **2015**, *21*, 1301–1305.
- (39) Davar, F.; Salavati-Niasari, M.; Fereshteh, Z. Synthesis and Characterization of SnO<sub>2</sub> Nanoparticles by Thermal Decomposition of New Inorganic Precursor. *J. Alloys Compd.* **2010**, *496*, 638–643.
- (40) Zinatloo-Ajabshir, S.; Mortazavi-Derazkola, S.; Salavati-Niasari, M. Nd<sub>2</sub>O<sub>3</sub>-SiO<sub>2</sub> Nanocomposites: A Simple Sonochemical Preparation, Characterization and Photocatalytic Activity. *Ultrason. Sonochem.* **2018**, *42*, 171–182.
- (41) Zinatloo-Ajabshir, S.; Salavati-Niasari, M. Preparation of Magnetically Retrievable CoFe<sub>2</sub>O<sub>4</sub>@SiO<sub>2</sub>@Dy<sub>2</sub>Ce<sub>2</sub>O<sub>7</sub> Nanocomposites as Novel Photocatalyst for Highly Efficient Degradation of Organic Contaminants. *Compos. Part B Eng.* **2019**, *174*, No. 106930.
- (42) Chan, W. C. W.; Maxwell, D. J.; Gao, X.; Bailey, R. E.; Han, M.; Nie, S. Luminescent Quantum Dots for Multiplexed Biological Detection and Imaging. *Curr. Opin. Biotechnol.* **2002**, *13*, 40–46.
- (43) Zhao, R.; Wang, Z.; Tian, X.; Shu, H.; Yang, Y.; Xiao, X.; Wang, Y. Excellent Fluorescence Detection of Cu<sup>2+</sup> in Water System Using N-Acetyl-L-Cysteines Modified CdS Quantum Dots as Fluorescence Probe. *Nanotechnology* **2021**, *32*, 405707.
- (44) Yang, W.; Li, X.; Fei, L.; Liu, W.; Liu, X.; Xu, H.; Liu, Y. A Review on Sustainable Synthetic Approaches toward Photoluminescent Quantum Dots. *Green Chem.* **2022**, *24*, 675–700.

- (45) Sabzehmeidani, M. M.; Kazemzad, M. Quantum Dots Based Sensitive Nanosensors for Detection of Antibiotics in Natural Products: A Review. *Sci. Total Environ.* **2022**, *810*, No. 151997.
- (46) Biranjeh, A.; Azmi, N.; Tiwari, A.; Chaskar, A. Quantum Dots Based Fluorescent Probe for the Selective Detection of Heavy Metal Ions. *J. Fluoresc.* **2021**, *31*, 1241–1250.
- (47) Bruchez, M., Jr.; Moronne, M.; Gin, P.; Weiss, S.; Alivisatos, A. P. Semiconductor Nanocrystals as Fluorescent Biological Labels. *Science* **1998**, *281*, 2013–2016.
- (48) Kim, A.; Hosseinmardi, A.; Annamalai, P. K.; Kumar, P.; Patel, R. Review on Colloidal Quantum Dots Luminescent Solar Concentrators. *ChemistrySelect* **2021**, *6*, 4948–4967.
- (49) Whaley, S. R.; English, D. S.; Hu, E. L.; Barbara, P. F.; Belcher, A. M. Selection of Peptides with Semiconductor Binding Specificity for Directed Nanocrystal Assembly. *Nature* **2000**, *405*, 665–668.
- (50) Yi, G.; Sun, B.; Yang, F.; Chen, D. Bionic Synthesis of ZnS:Mn Nanocrystals and Their Optical Properties. *J. Mater. Chem.* **2001**, *11*, 2928–2929.
- (51) Mitchell, G. P.; Mirkin, C. A.; Letsinger, R. L. Programmed Assembly of DNA Functionalized Quantum Dots. *J. Am. Chem. Soc.* **1999**, *121*, 8122–8123.
- (52) Zhou, J.; Yang, Y.; Zhang, C. Toward Biocompatible Semiconductor Quantum Dots: From Biosynthesis and Bioconjugation to Biomedical Application. *Chem. Rev.* **2015**, *115*, 11669–11717.
- (53) Jiang, R.; Zhu, H.; Li, X.; Xiao, L. Visible Light Photocatalytic Decolourization of C. I. Acid Red 66 by Chitosan Capped CdS Composite Nanoparticles. *Chem. Eng. J.* **2009**, *152*, 537–542.
- (54) Abdelhamid, H. N.; El-Bery, H. M.; Metwally, A. A.; Elshazly, M.; Hathout, R. M. Synthesis of CdS-Modified Chitosan Quantum Dots for the Drug Delivery of Sesamol. *Carbohydr. Polym.* **2019**, *214*, 90–99.
- (55) Jiang, R.; Zhu, H.-Y.; Fu, Y.-Q.; Jiang, S.-T.; Zong, E.-M.; Zhu, J.-Q.; Zhu, Y.-Y.; Chen, L.-F. Colloidal CdS Sensitized Nano-ZnO/Chitosan Hydrogel with Fast and Efficient Photocatalytic Removal of Congo Red under Solar Light Irradiation. *Int. J. Biol. Macromol.* **2021**, *174*, 52–60.
- (56) Mansur, H. S.; Mansur, A. A. P.; Curti, E.; De Almeida, M. V. Bioconjugation of Quantum-Dots with Chitosan and N,N,N-Trimethyl Chitosan. *Carbohydr. Polym.* **2012**, *90*, 189–196.
- (57) Santos, J.; Mansur, A.; Mansur, H. One-Step Biofunctionalization of Quantum Dots with Chitosan and N-Palmitoyl Chitosan for Potential Biomedical Applications. *Molecules* **2013**, *18*, 6550–6572.
- (58) Liu, N.; Tang, M. Toxicity of Different Types of Quantum Dots to Mammalian Cells in Vitro: An Update Review. *J. Hazard. Mater.* **2020**, *399*, No. 122606.
- (59) Yu, W. W.; Qu, L.; Guo, W.; Peng, X. Experimental Determination of the Extinction Coefficient of CdTe, CdSe, and CdS Nanocrystals. *Chem. Mater.* **2003**, *15*, 2854–2860.
- (60) Focher, B.; Beltrame, P. L.; Naggi, A.; Torri, G. Alkaline N-Deacetylation of Chitin Enhanced by Flash Treatments. Reaction Kinetics and Structure Modifications. *Carbohydr. Polym.* **1990**, *12*, 405–418.
- (61) Zhang, Y.; Xue, C.; Xue, Y.; Gao, R.; Zhang, X. Determination of the Degree of Deacetylation of Chitin and Chitosan by X-Ray Powder Diffraction. *Carbohydr. Res.* **2005**, *340*, 1914–1917.
- (62) Li, Z.; Du, Y.; Zhang, Z.; Pang, D. Preparation and Characterization of CdS Quantum Dots Chitosan Biocomposite. *React. Funct. Polym.* **2003**, *55*, 35–43.
- (63) Rhazi, M.; Desbrières, J.; Tolaimate, A.; Rinaudo, M.; Vottero, P.; Alagui, A.; El Meray, M. Influence of the Nature of the Metal Ions on the Complexation with Chitosan. *Eur. Polym. J.* **2002**, *38*, 1523–1530.
- (64) Yadav, A. N.; Kumar, P.; Singh, K. Femtosecond Photoluminescence Up-Conversion Spectroscopy in Cu Doped CdS Quantum Dots. *Mater. Lett.* **2021**, *297*, No. 129925.
- (65) Abdelhamid, H. N.; Goda, M. N.; Said, A. E.-A. A. Selective Dehydrogenation of Isopropanol on Carbonized Metal–Organic Frameworks. *Nano-Structures & Nano-Objects* **2020**, *24*, No. 100605.
- (66) Lai, S.; Chang, X.; Fu, C. Cadmium Sulfide Quantum Dots Modified by Chitosan as Fluorescence Probe for Copper (II) Ion Determination. *Microchim. Acta* **2009**, *165*, 39–44.